RESEARCH ARTICLE

Figures and figure supplements

Myosin V executes steps of variable length via structurally constrained diffusion

David Hathcock *et al*

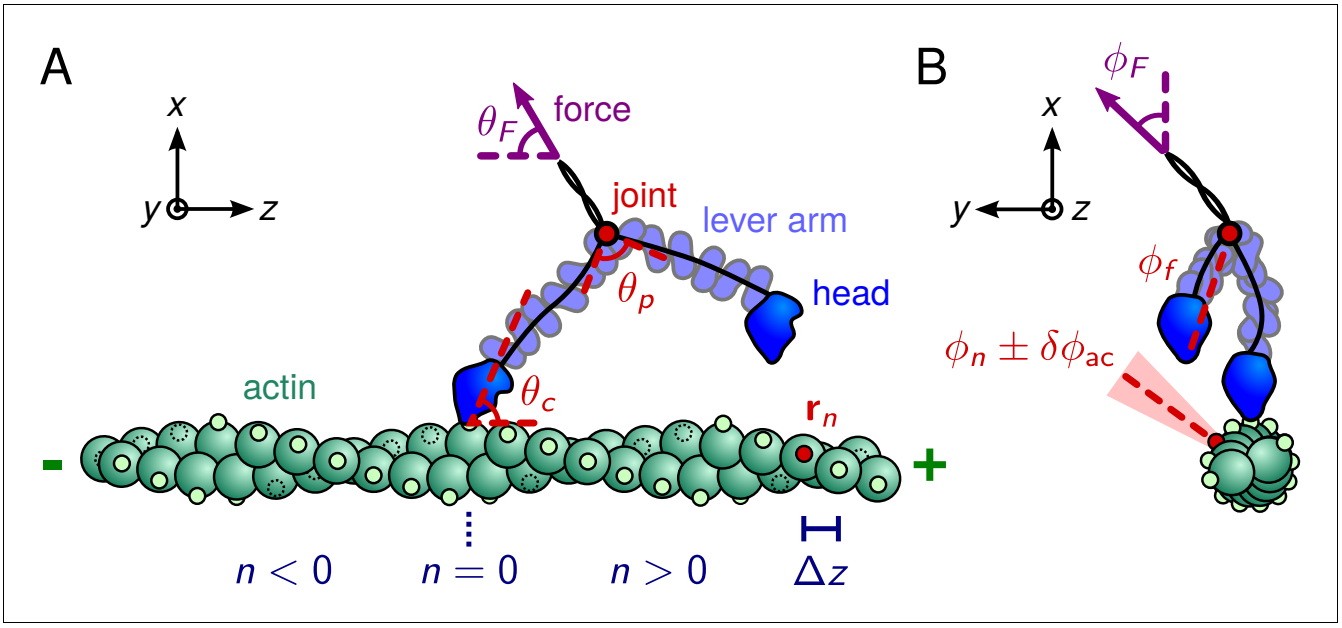

Figure 1. Myosin V geometry. (**A**) Side view, with the actin filament plus end oriented toward the $\hat{\mathbf{z}}$ direction. Small circles on the actin monomers denote the binding sites $\mathbf{r}_n$, described by ***Equation 1***. The site $n = 0$ corresponds to the position of the bound head. The bound polymer leg has a preferred post-power stroke direction in the $x - z$ plane defined by a constraint angle θ_c relative to the $\hat{\mathbf{z}}$ axis. Due to the hypothesized structural constraint at the joint, the preferred angle between the lever arms is θ_p. The force transmitted through the tail domain has a polar angle θ_F relative to the $-\hat{\mathbf{z}}$ direction. (**B**) Front view, with the actin plus end pointing out of the page. Each binding site has an associated outward pointing normal direction with azimuthal angle ϕ_n. As an example, one such angle is shown for the red-colored site. All azimuthal angles are measured counter-clockwise with respect to the $\hat{\mathbf{x}}$ direction. For binding to occur, the head has to be in the vicinity of the site, and oriented approximately along the normal. We approximately capture this condition by a binding criterion that requires the azimuthal angle of the free leg, ϕ_f, to be anti-parallel to ϕ_n within a cutoff range $\pm\delta\phi_{ac}$, highlighted in light red. The load force may have an off-axis component with azimuthal angle ϕ_F.

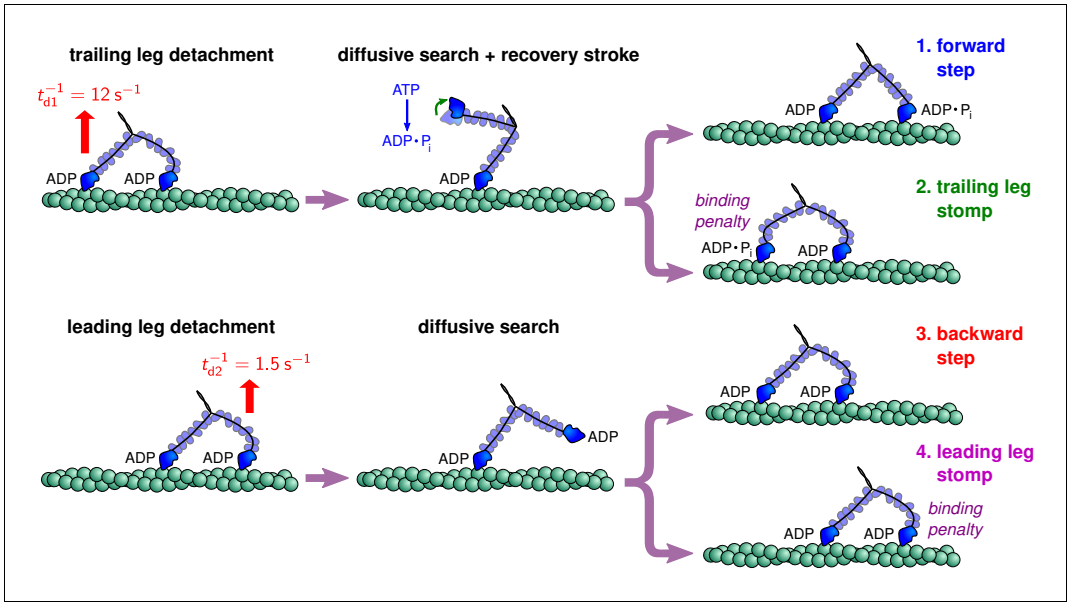

Figure 2. Myosin V kinetic pathways.

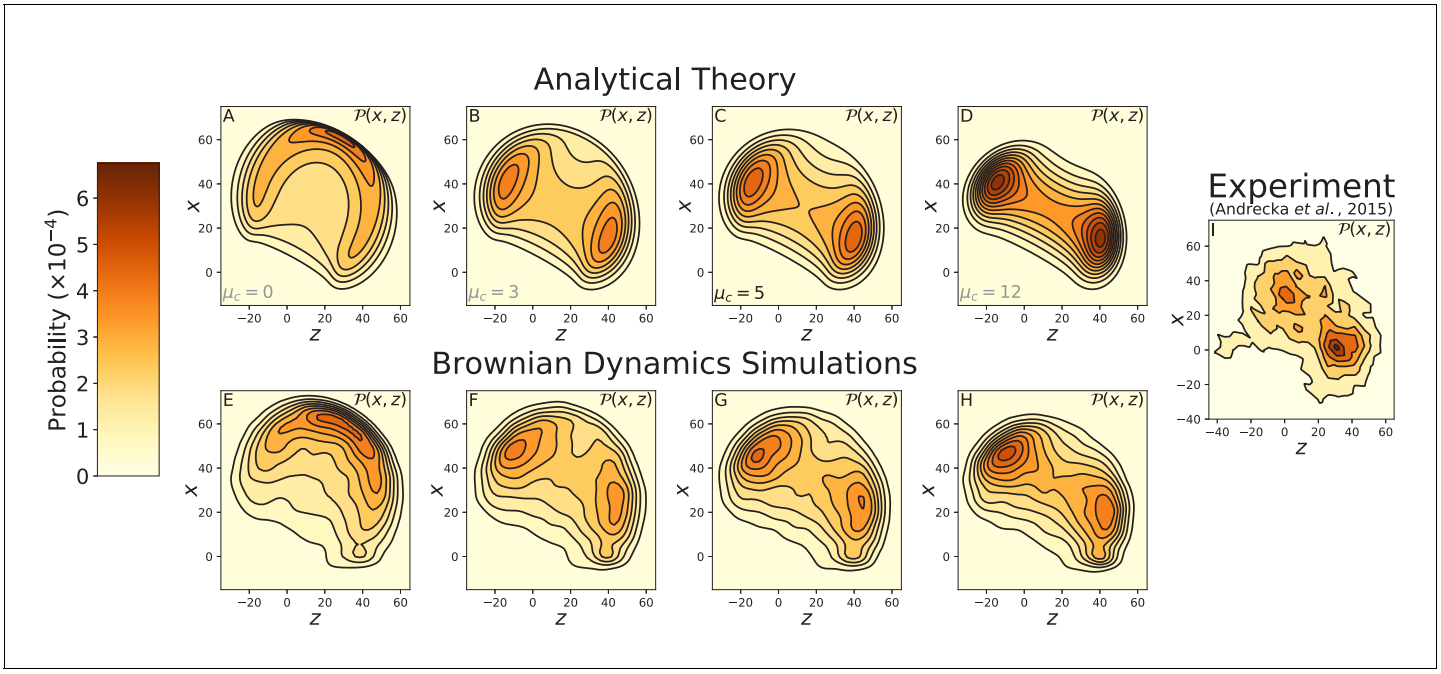

Figure 3. Contours of the myosin V free head position distribution $\mathcal{P}(\mathbf{r})$ projected onto the $z-x$ plane. Top row: theoretical predictions for (**A**) free diffusion ($\mu_c = 0$) and (**B–D**) constrained diffusion with inter-leg constraint strength (**B**) $\mu_c = 3$, (**C**) $\mu_c = 5$, and (**D**) $\mu_c = 12$. Bottom row: the corresponding contours measured from Brownian dynamics simulations, with inter-leg constraint strength (**E**) $\mu_c = 0$, (**F**) $\mu_c = 3$, (**G**) $\mu_c = 5$, and (**H**) $\mu_c = 12$. (**I**) Experimental measurements of the diffusion by ***Andrecka et al. (2015)***. Adding an inter-leg constraint potential produces a multi-peaked diffusion pattern. The heights of the peaks are similar to the experimental measurements for $3 \lesssim \mu_c \lesssim 12$. Note that the $x = 0$ axis in the experimental data corresponds to the position of the gold bead attached to the myosin head when the head is bound to actin. Given the ~5 nm size of the head and ~10 nm radius of the bead, this accounts for the approximately 15 nm vertical shift between the theoretical/simulation distributions and experiment. In the former the $x = 0$ axis corresponds to the top of the actin filament (where the bound head is attached).

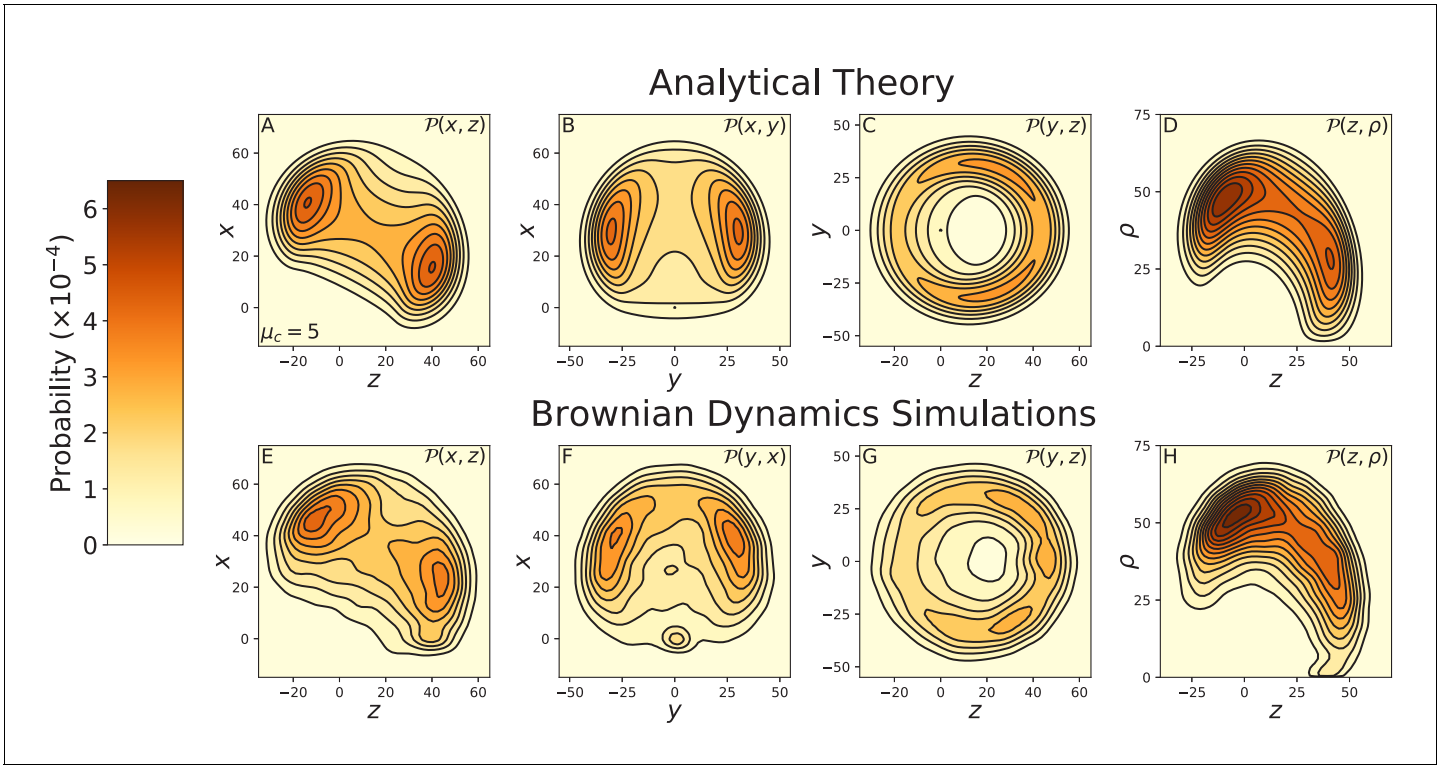

Figure 3—figure supplement 1. Alternative projections of the constrained diffusion ($\mu_c = 5$). Top row: theoretical calculations of the diffusion projected onto the (**A**) $z - x$, (**B**) $y - x$, and (**C**) $z - y$ planes, and (**D**) the cylindrical plane $z - \rho$. Bottom row: diffusion contours measured from Brownian dynamics simulations, again projected onto the (**E**) $z - x$, (**F**) $y - x$, and (**G**) $z - y$ planes, and (**H**) the cylindrical plane $z - \rho$. Agreement between theory and simulations is excellent.

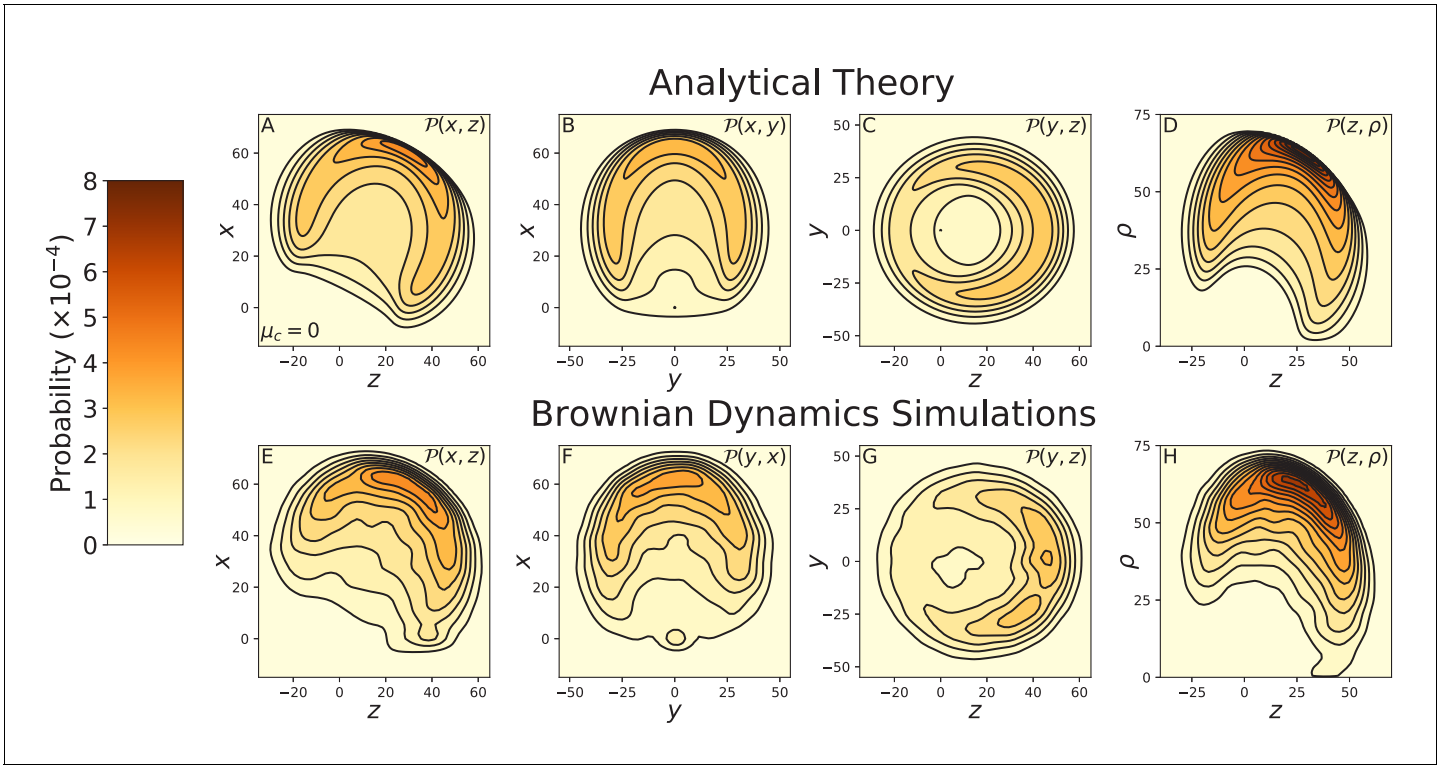

Figure 3—figure supplement 2. Alternative projections of the free diffusion ($\mu_c = 0$). Top row: theoretical calculations of the diffusion projected onto the (**A**) $z - x$, (**B**) $y - x$, and (**C**) $z - y$ planes, and (**D**) the cylindrical plane $z - \rho$. Bottom row: diffusion contours measured from Brownian dynamics simulations, again projected onto the (**E**) $z - x$, (**F**) $y - x$, and (**G**) $z - y$ planes, and (**H**) the cylindrical plane $z - \rho$. In the analytical theory we include a joint Hamiltonian that penalizes small inter-leg angles. This mimics the effects of steric repulsion between the legs, which are explicitly included in the BD simulations. With this adjustment to the theory, agreement between the theory and simulations is excellent.

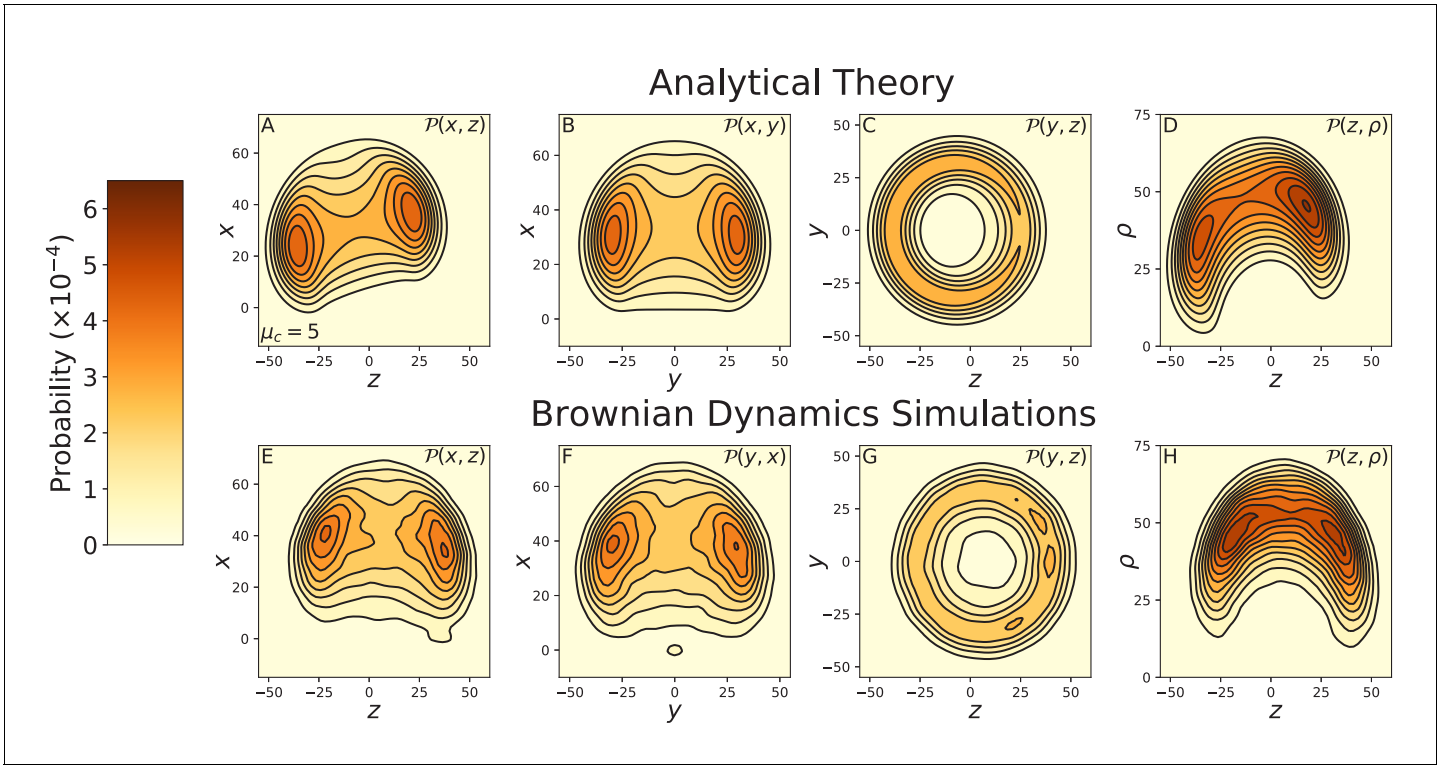

Figure 3—figure supplement 3. Constrained diffusion of myosin V under 2 pN backward force. The constraint strength was set to $\mu_c = 5$. The force F = 2 pN is in the stall regime, just above the stall force. Top row: theoretical calculations of the diffusion projected onto the (**A**) $z - x$, (**B**) $y - x$, and (**C**) $z - y$ planes, and (**D**) the cylindrical plane $z - \rho$. Bottom row: diffusion contours measured from Brownian dynamics simulations, again projected onto the (**E**) $z - x$, (**F**) $y - x$, and (**G**) $z - y$ planes, and (**H**) the cylindrical plane $z - \rho$. The theory and simulations agree qualitatively, showing the diffusion is rotated toward the minus end of the actin compared to that at zero load (***Figure 3—figure supplement 1***). Quantitative discrepancies are primarily due to a small difference in the stall force between the theoretical and numerical models.

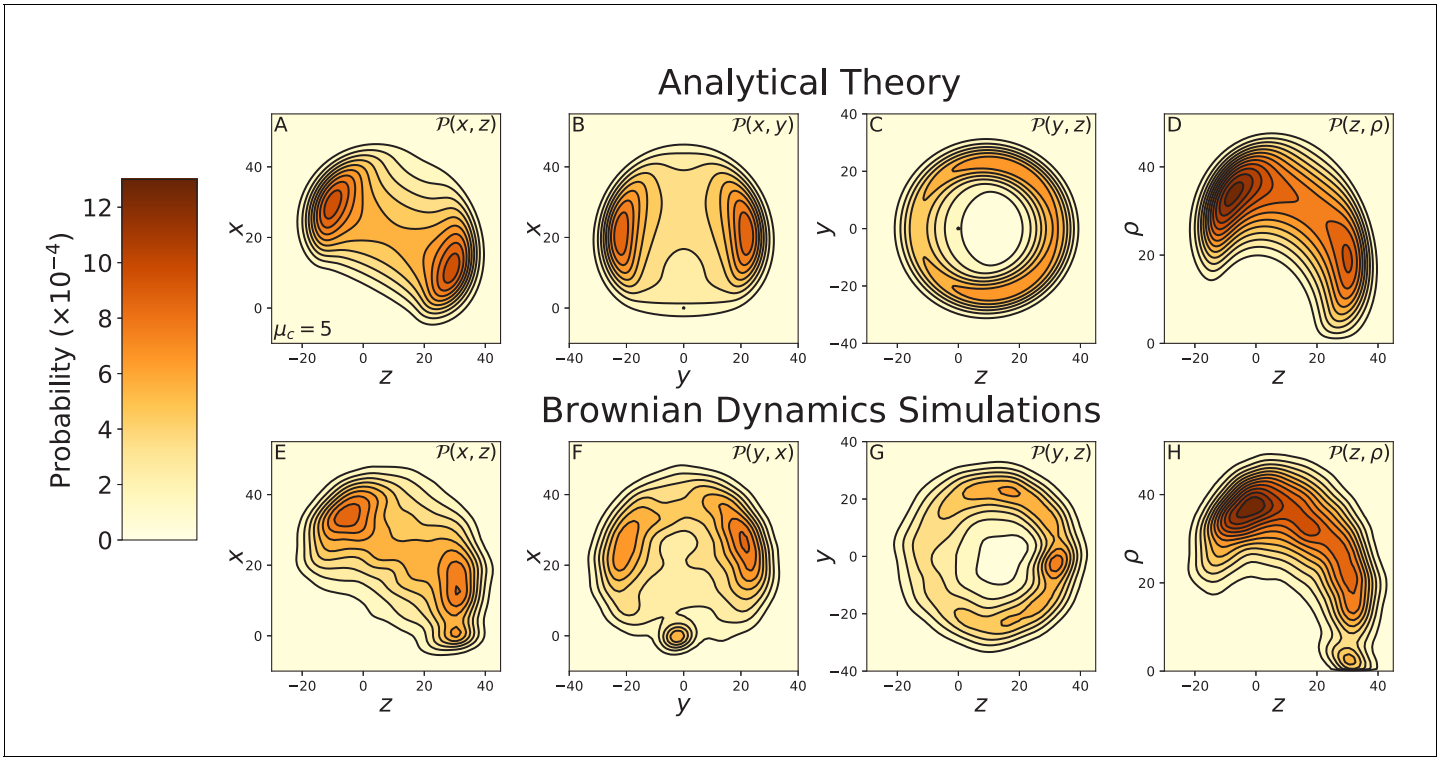

Figure 3—figure supplement 4. Constrained diffusion of the 4IQ myosin mutant. The constraint strength was set to $\mu_c = 5$. Top row: theoretical calculations of the diffusion projected onto the (**A**) $z-x$, (**B**) $y-x$, and (**C**) $z-y$ planes, and (**D**) the cylindrical plane $z-\rho$. Bottom row: diffusion contours measured from Brownian dynamics simulations, again projected onto the (**E**) $z-x$, (**F**) $y-x$, and (**G**) $z-y$ planes, and (**H**) the cylindrical plane $z-\rho$. Notice the difference in probability and length scales in this figure versus those preceding. The 4IQ mutant has a nearly identical diffusion pattern to the wild-type myosin, scaled down due to the decreased lever arm length.

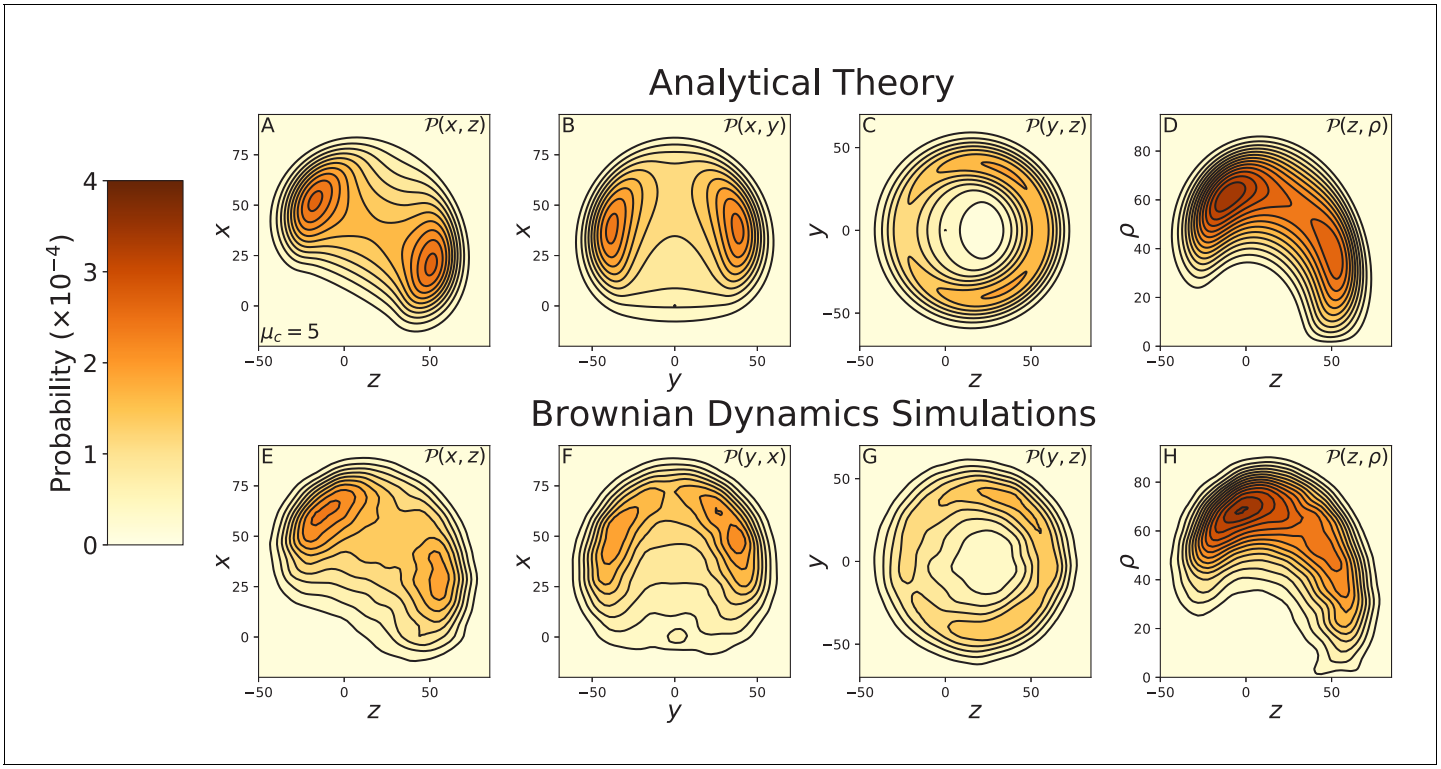

Figure 3—figure supplement 5. Constrained diffusion of the 8IQ myosin mutant. The constraint strength was set to $\mu_c = 5$. Top row: theoretical calculations of the diffusion projected onto the (**A**) $z - x$, (**B**) $y - x$, and (**C**) $z - y$ planes, and (**D**) the cylindrical plane $z - \rho$. Bottom row: diffusion contours measured from Brownian dynamics simulations, again projected onto the (**E**) $z - x$, (**F**) $y - x$, and (**G**) $z - y$ planes, and (**H**) the cylindrical plane $z - \rho$. Notice the difference in probability and length scales in this figure versus those preceding. The 8IQ mutant has a nearly identical diffusion pattern to the wild-type myosin, scaled up due to the increased lever arm length.

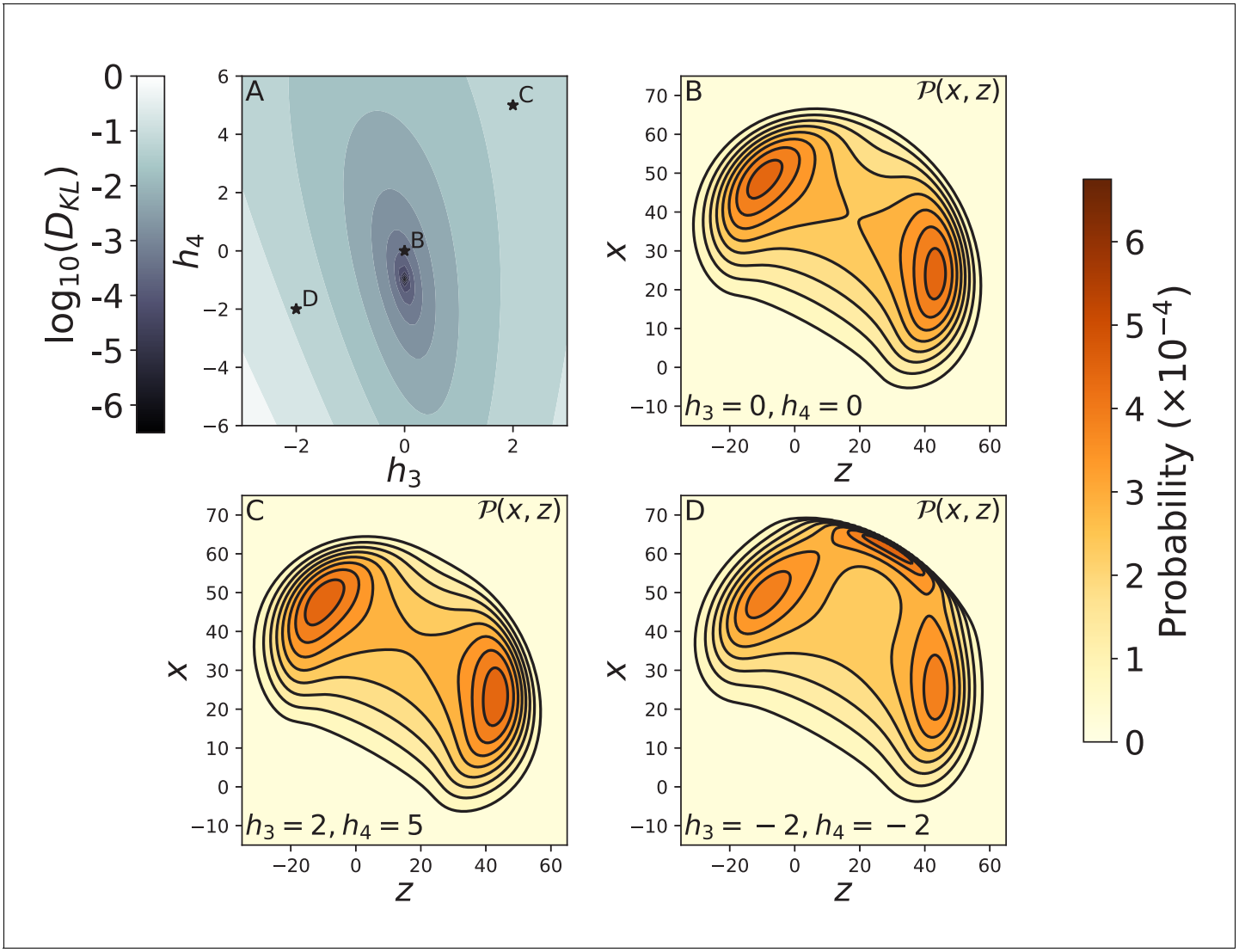

Figure 3—figure supplement 6. Effect of the form of the joint potential on free head diffusion. (**A**) The log of the KL divergence $D_{KL}(\mathcal{P}_{\cos}|\mathcal{P})$ between the free head spatial probability densities $\mathcal{P}_{\cos}(\mathbf{r})$ and $\mathcal{P}(\mathbf{r})$ corresponding to the cosine potential used in the main text and $H_J = \mu_c k_B T[(\Delta\theta)^2/2 + h_3(\Delta\theta)^3/3! + h_4(\Delta\theta)^4/4!]$ respectively. The minimum KL divergence occurs at $(h_3, h_4) = (0, 1)$, which is the quartic expansion of the cosine potential. The stars indicate the potentials used to compute diffusion contours in panels **B–D**. The $x - z$ diffusion contours are shown for (**B**) the harmonic potential ($h_3 = h_4 = 0$), as well as potentials with (**C**) $(h_3, h_4) = (2, 4)$, and (**D**) $(h_3, h_4) = (-2, -2)$. The harmonic potential produces diffusion that is nearly identical to the cosine potential (***Figure 3C***), while the contour shown in **C** has only subtle differences. The diffusion shown in **D** is qualitatively different because the potential has an additional energy minimum giving rise to a new peak in the distribution. In all cases we set $\mu_c = 5$, as in the main text.

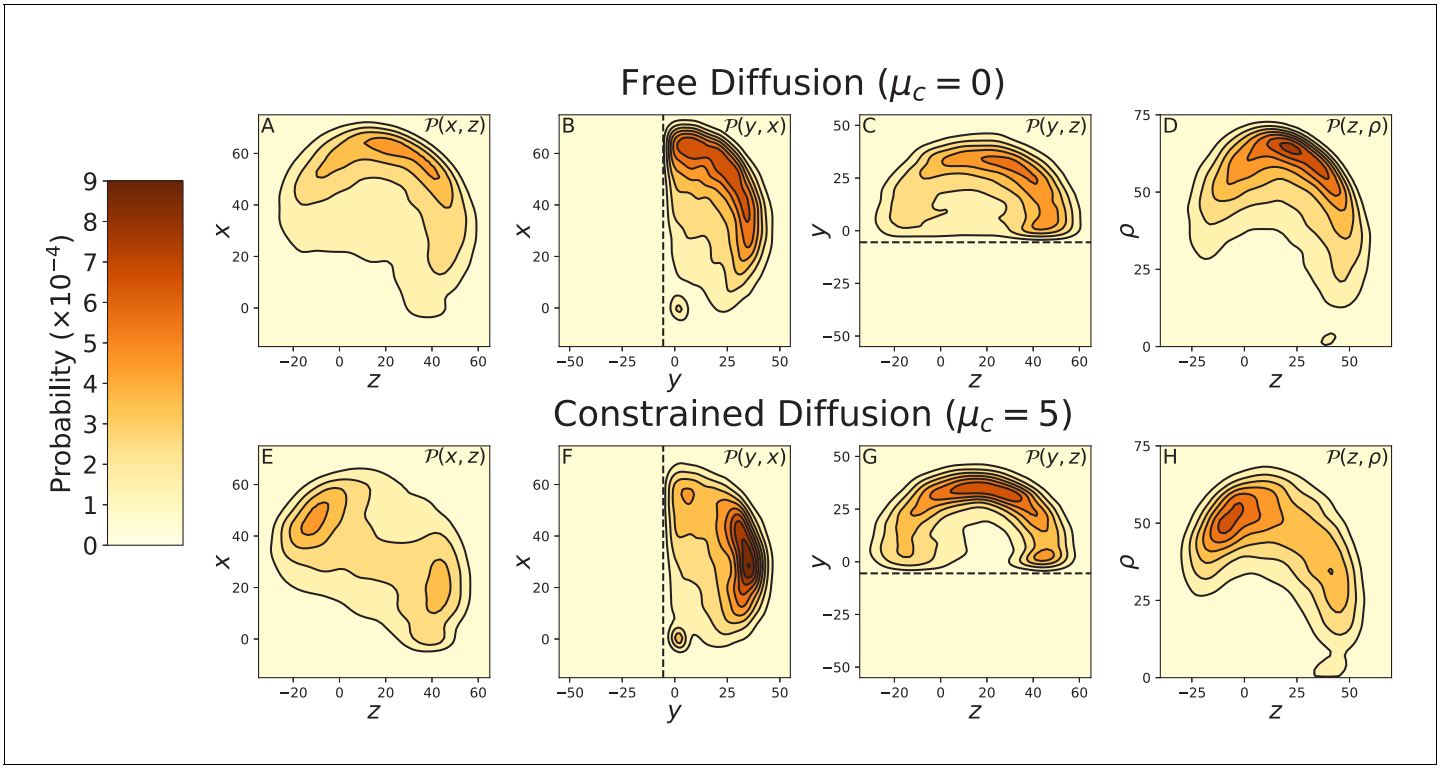

Figure 3—figure supplement 7. Effects of cover-slip volume exclusion on diffusion. Data was taken using Brownian Dynamics simulations with a glass cover-slip cutting off half the 3-dimensional space, modeled with a soft-core repulsive potential as described in Appendix 2. The cover-slip is at y = —5.5 nm, parallel to the $x-z$ plane and is indicated by the dashed line in the relevant diffusion projections. Top row: BD simulations of free diffusion ($\mu_c = 0$), projected onto the (**A**) $z-x$, (**B**) $y-x$, and (**C**) $z-y$ planes, and (**D**) the cylindrical plane $z-\rho$. Bottom row: BD simulations of free diffusion ($\mu_c = 5$), again projected onto the (**E**) $z-x$, (**F**) $y-x$, and (**G**) $z-y$ planes, and (**H**) the cylindrical plane $z-\rho$. The $z-x$ diffusion contour is not considerably altered by the cover-slip in both the free and constrained diffusion models. Therefore, the multi-peaked contour measured by ***Andrecka et al. (2015)*** is not an artifact of entropic forces due to volume exclusion.

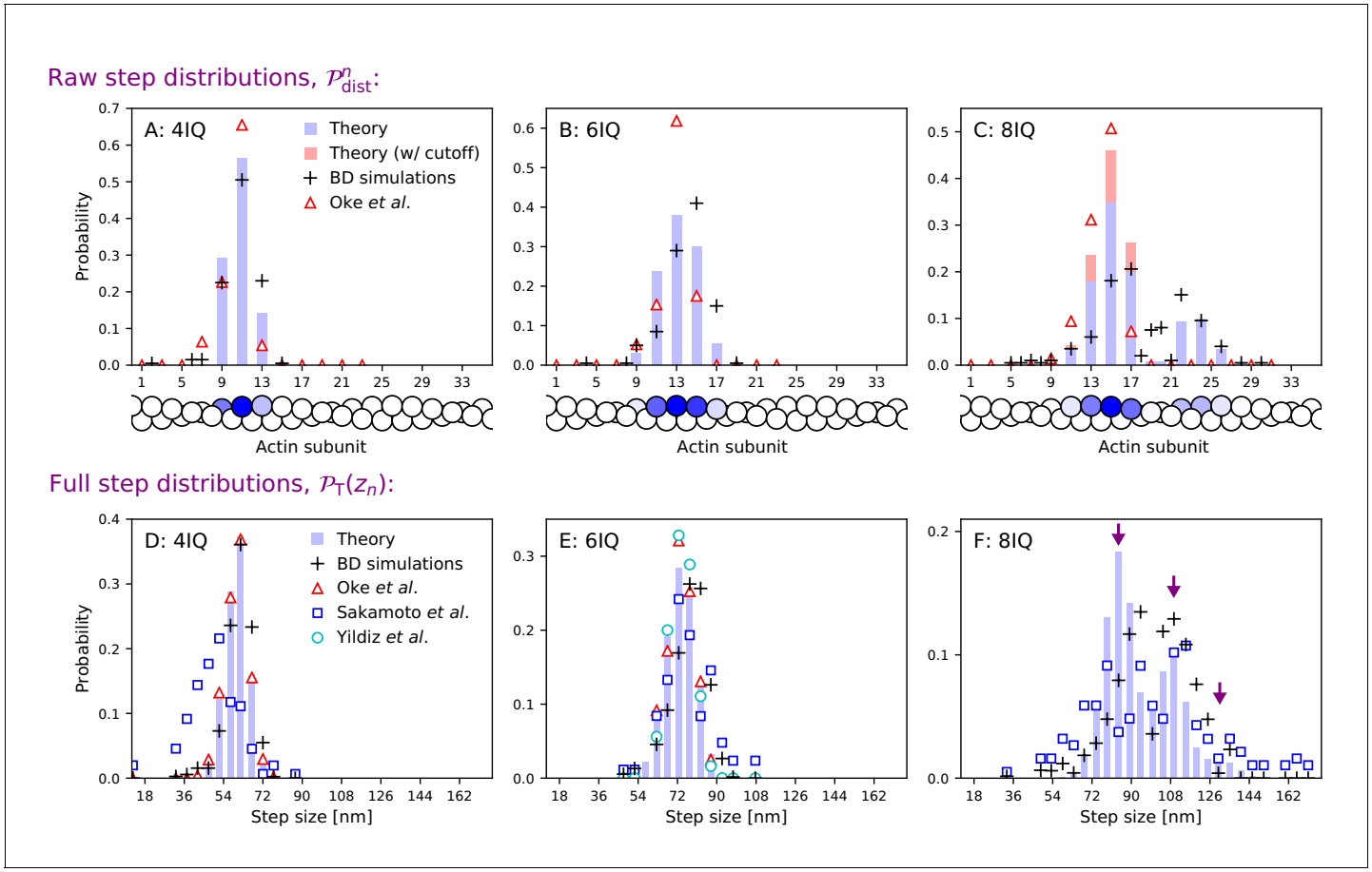

Figure 4. Step size distributions for myosin V and mutants with altered leg length. Top row: raw step distributions for (**A**) the 4IQ mutant, (**B**) the 6IQ wild-type, and (**C**) the 8IQ mutant. Bottom row: full (convolved) step distributions for (**D**) the 4IQ mutant, (**E**) the 6IQ wild-type, and (**F**) the 8IQ mutant, with three theoretical peak locations indicated by arrows. Theoretical distributions are shown as histograms with Brownian dynamics simulations and experimental data from ***Oke et al. (2010)***, ***Sakamoto et al. (2005)***, and ***Yildiz et al. (2003)*** indicated by symbols. The raw data from ***Oke et al. (2010)*** is convolved and binned in the bottom row. Since the imaging methods used in this experiment did not resolve large steps taken by the 8IQ mutant, in panel C we show an alternative theory (in red) with a cutoff where only small steps are allowed. The actin monomers drawn below the top row are shaded according to the analytical theory results, with the darkest color normalized to the peak of the distribution.

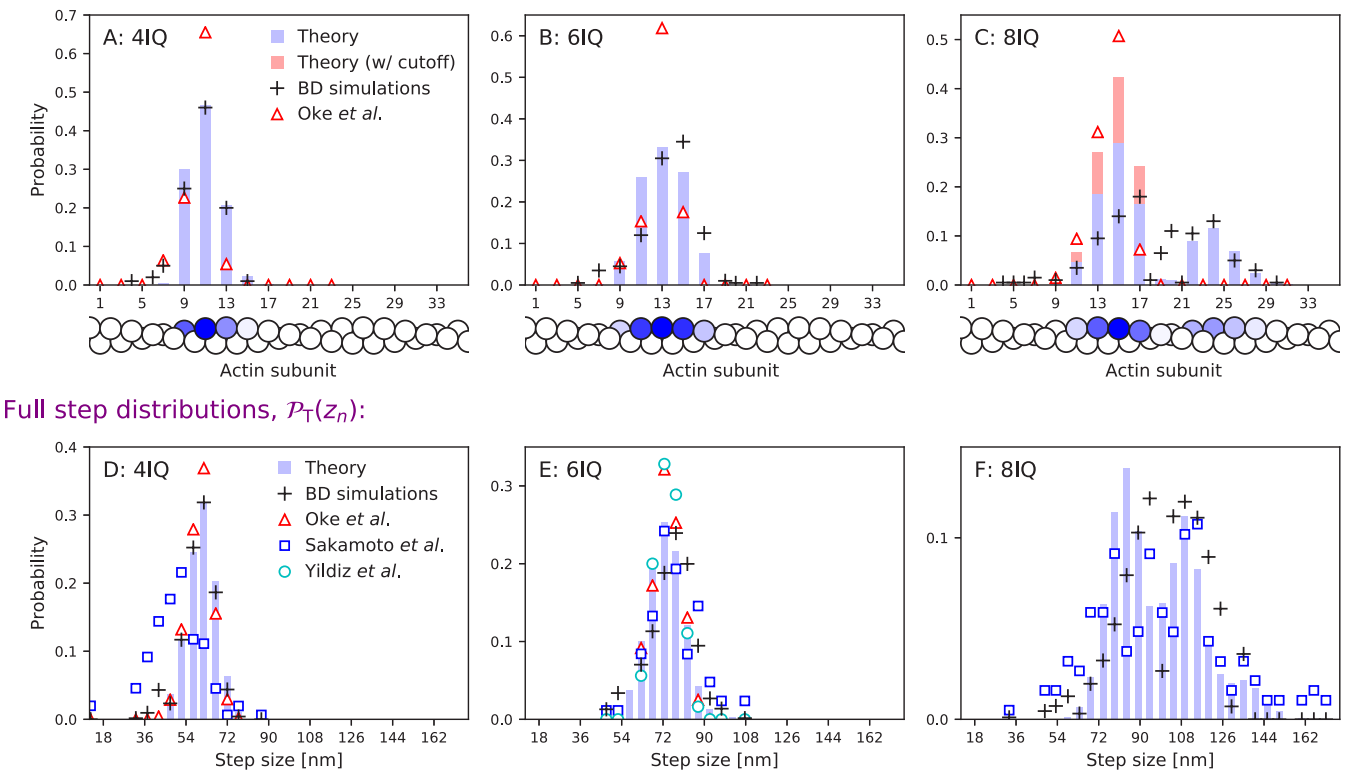

Figure 4—figure supplement 1. Step distributions for myosin V and mutants with a freely rotating inter-leg joint. Same as ***Figure 4***, but analytical theory and Brownian dynamics simulations used the free diffusion model. The analytical model was fit to data using the procedure described in the main text. We used parameters: $l_p = 320\,\mathrm{nm}$, $\theta_c = 59.7°$, $\nu_c = 140$, $\mu_c = 0$, $a = 0.3\,\mathrm{nm}$, $b = 0.07$, and $\delta\phi_{\mathrm{ac}} = 57.0°$, with all other parameters identical to ***Table 2***. Agreement with experimental measurements is comparable to that for the constrained diffusion model.

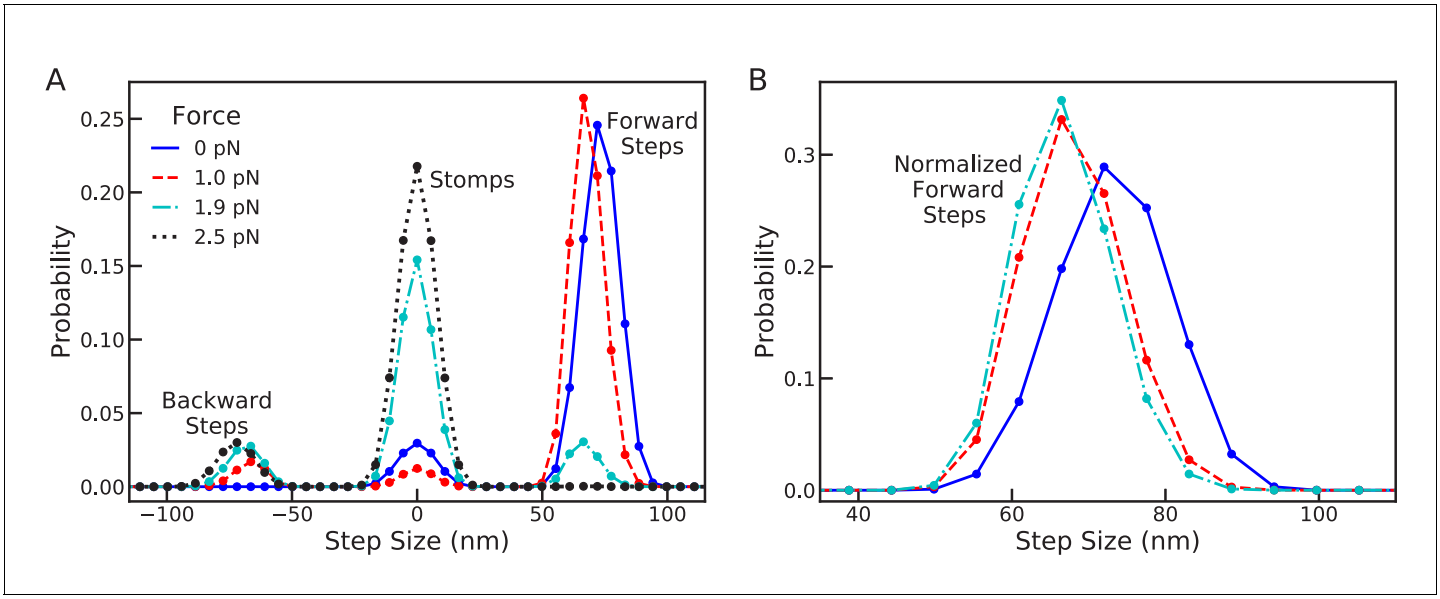

Figure 5. Changes in the full step distribution, including leading and trailing leg contributions, under backward load. (**A**) Distributions for zero force F = 0 pN (solid line), sub-stall force F = 1 pN (dashed line), stall force F = 1.9 pN (dot-dashed line), and super-stall force F = 2.5 pN (dotted line). The peaks near 72 nm, 0 nm and – 72 nm correspond to forward steps, stomps, and backward steps respectively. Applying force shifts the forward step distribution backward slightly (by about 1 actin subunit) and increases the probability of stomps and backward steps. (**B**) Normalized forward step distributions for F = 0 pN, F = 1 pN, and F = 1.9 pN. Even when other kinetic pathways are dominant the shape of the forward step distribution remains robust to load force.

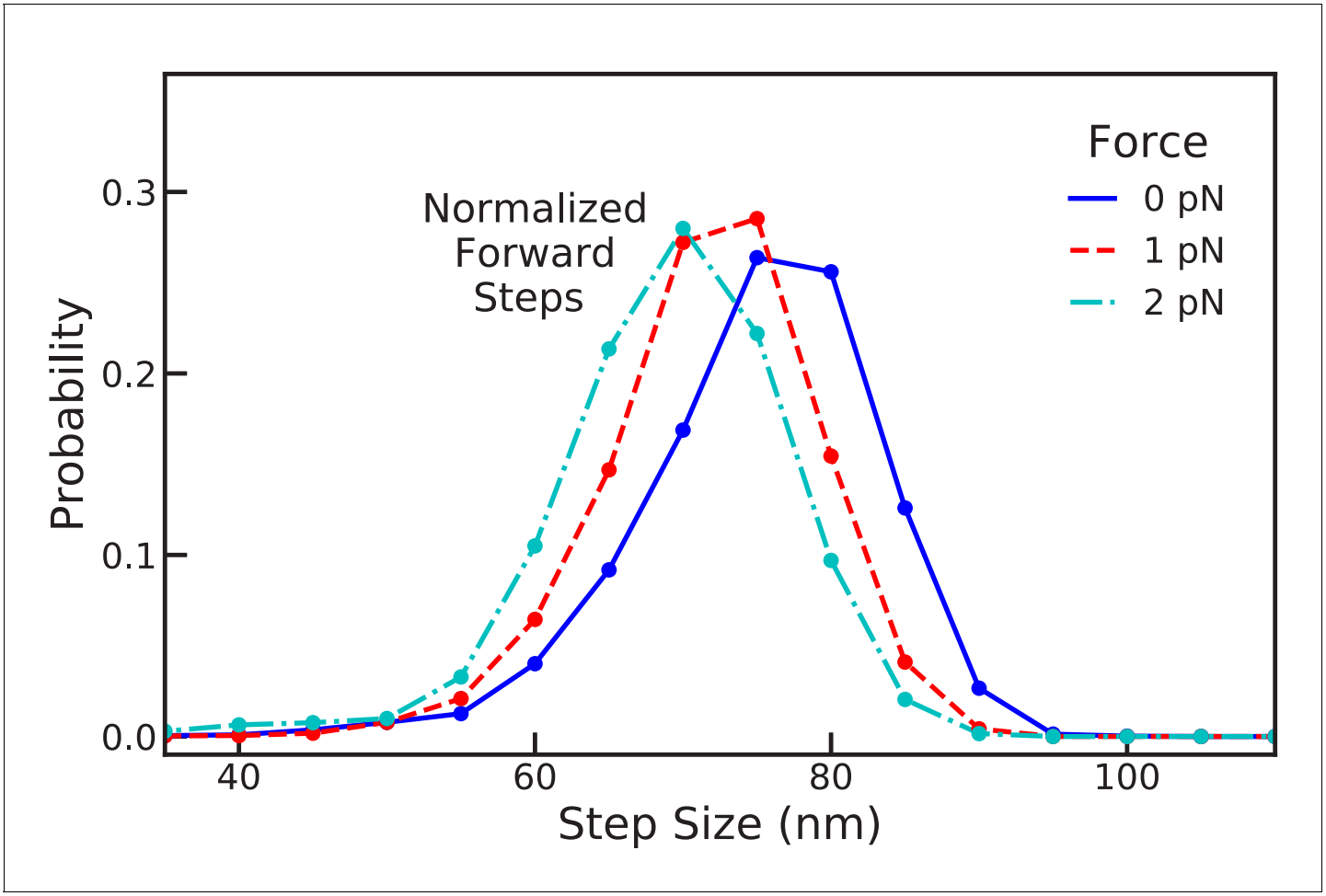

Figure 5—figure supplement 1. Robust forward step distributions from Brownian dynamics simulations. Shown are the normalized forward step distribution measured from BD trajectories with zero force and under backward load of 1 pN and 2 pN. The distribution is fairly robust, shifting back about one actin subunit per piconewton of applied force, in qualitative agreement with the analytical model (***Figure 5B***).

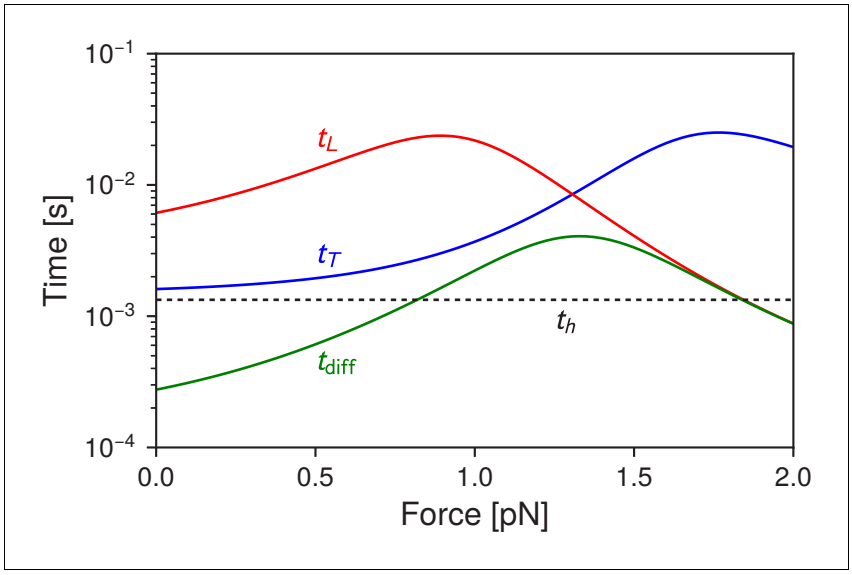

Figure 6. Myosin V timescales as a function of F, the backward load force. t_{diff} is the mean timescale for the detached head to diffuse within radius a of any of the actin binding sites. t_T and t_L are the mean times for the trailing and leading heads to bind after detachment. For comparison, t_h is the mean timescale of ATP hydrolysis.

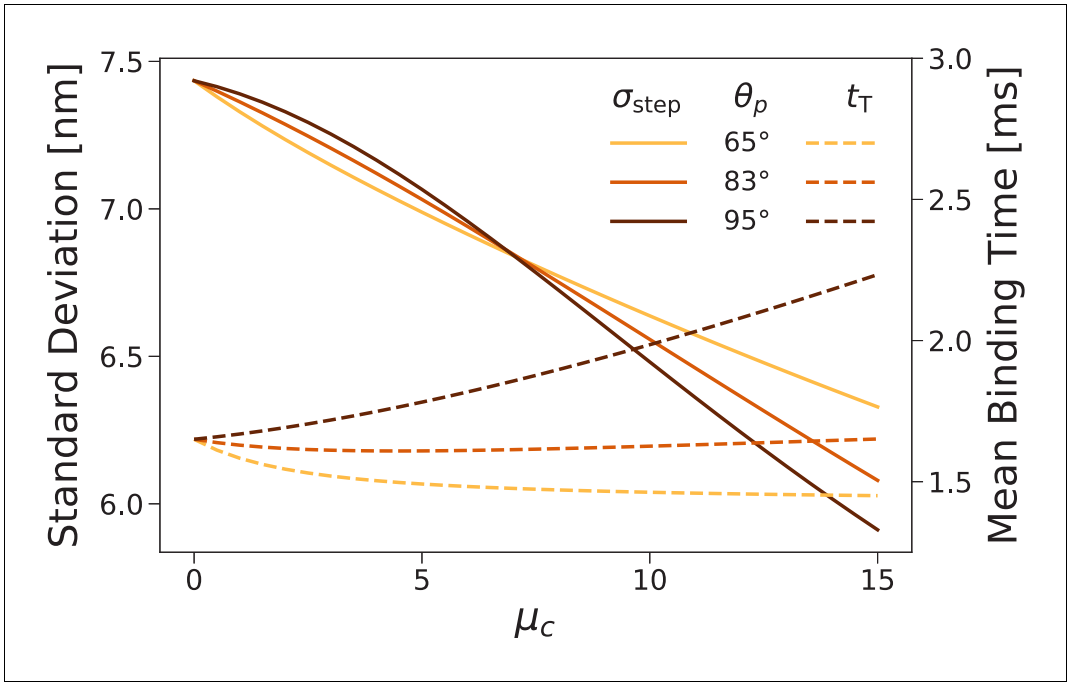

Figure 7. Forward step distribution width (solid lines) and mean binding time after trailing leg detachment (dashed lines) for $F = 0$ as a function of the inter-leg constraint strength μ_c. We carried out this calculation for $\theta_p = 83°$ (the value used throughout this paper) as well as $\theta_p = 65°$ and $95°$. As the constraint is increased the step distribution narrows, while changes in the binding time are relatively small.

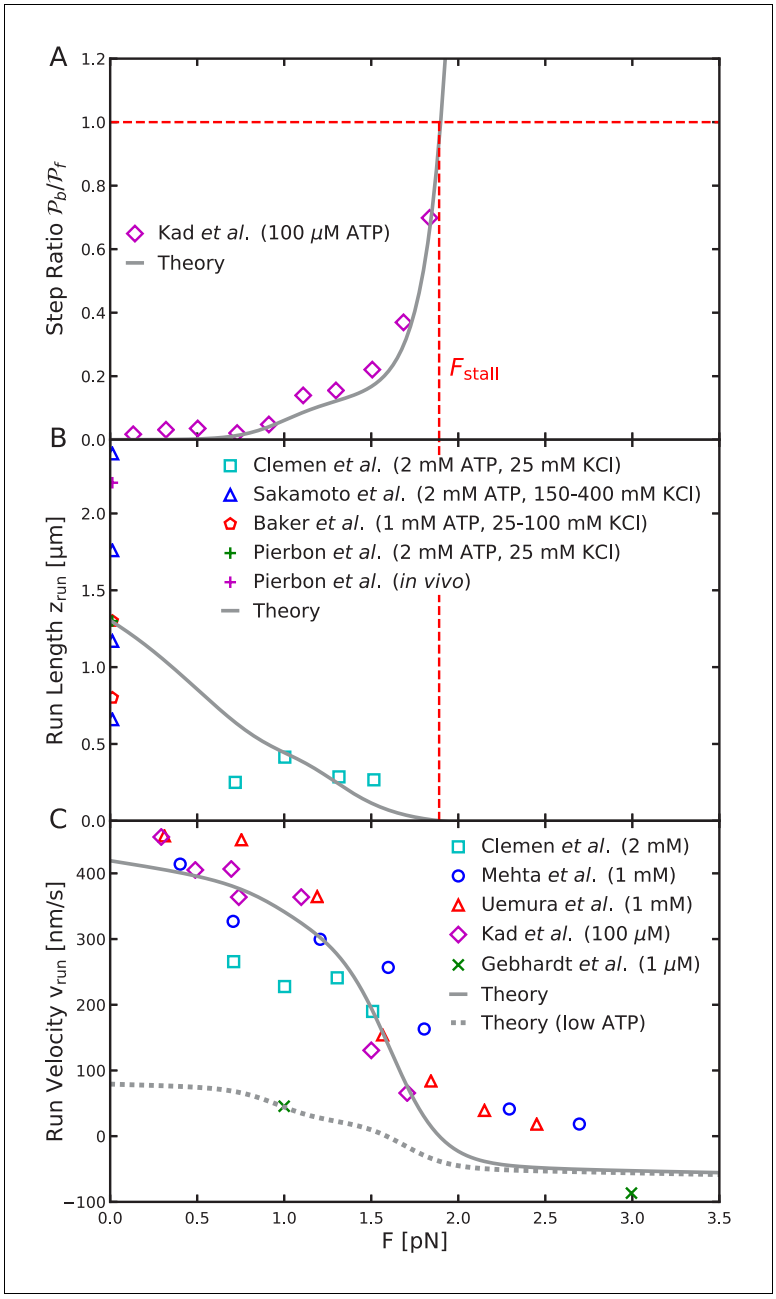

Figure 8. Load-dependent aspects of myosin V dynamics. (**A**) Backward-to-forward step ratio $\mathcal{P}_b/\mathcal{P}_f$; (**B**) mean run length $z_{\rm run}$; (**C**) mean run velocity $v_{\rm run}$. Analytical theory results are drawn as curves, experimental results as symbols. The legend symbols are the same as those in ***Hinczewski et al. (2013)***, for ease of comparison, but the theory curves have been updated.

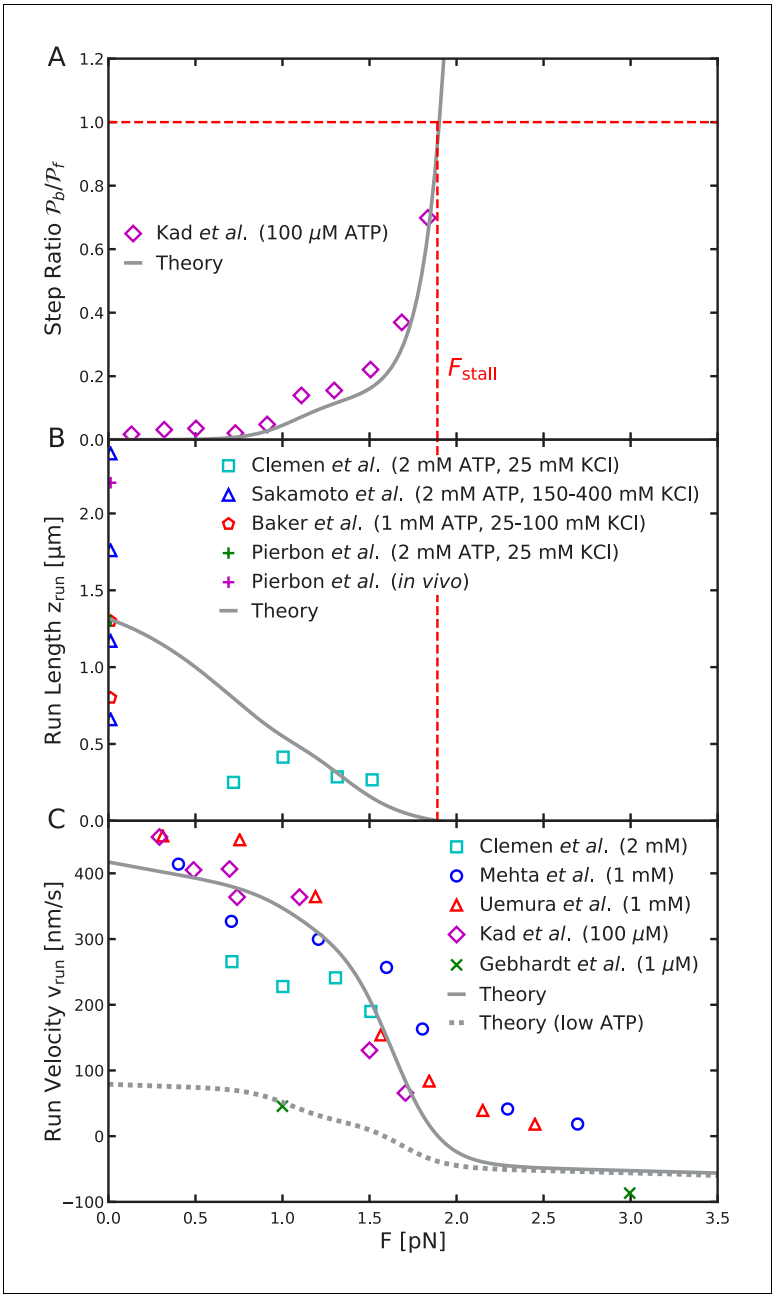

Figure 8—figure supplement 1. Load-dependence of step ratio, run length, and run velocity is captured by the free diffusion model. Same as ***Figure 8***, but using the analytical free diffusion model, fit to experiments as described in the main text. We used parameters: $l_p = 320\,\mathrm{nm}$, $\theta_c = 59.7°$, $\nu_c = 140$, $\mu_c = 0$, $a = 0.3\,\mathrm{nm}$, $b = 0.07$, and $\delta\phi_{ac} = 57.0°$, with all other parameters identical to ***Table 2***. Agreement with experimental measurements is comparable to that for the constrained diffusion model.

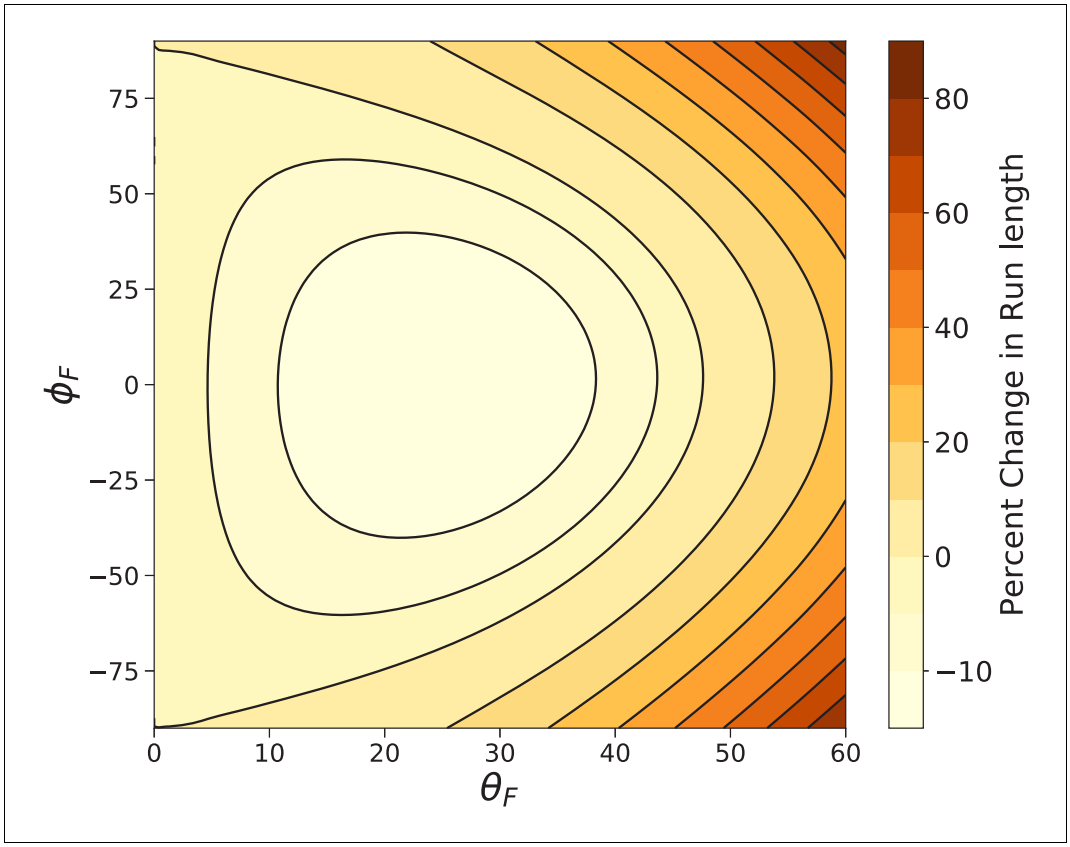

Figure 9. Myosin V run length under off-axis forces. Shown is the percent change in run length from that under backward force $z_{\mathrm{run}}(\theta_F, \phi_F)/z_{\mathrm{run}}(0,0) - 1$ computed using ***Equation 9***. In the worst case ($\theta_F \approx 20°, \phi_F = 0$) the run length is decreased by $\sim 15\%$. The run length most dramatically increases under fully off-axis forces ($\theta_F > 0, \phi_F = \pm 90°$).